Published in Journal of Electroceramics, DOI: 10.1007/s10832-025-00384-2, 09 January 2025

Investigation of Structural, Electronic, and Optical Properties of Er-Doped KNN System Based on First-Principles Calculations

Zhichao Gong[1] · Haojie Yue[1] · Kailing Fang[1] · Kun Guo[1,*] · Bing Xie[1] · Zhiyong Liu[1] · Pu Mao[1] · Jinshan Lu[1] · Kui Yao[2] · Francis Eng Hock Tay[3]

[1]*School of Power and Energy, Nanchang Hangkong University, Nanchang 330063, China*

[2]*Institute of Materials Research and Engineering, A*STAR (Agency for Science, Technology and Research), 2 Fusionopolis Way, 138634, Singapore,*

[3]*Department of Mechanical Engineering, National University of Singapore, 9 Engineering Drive 1, 117575, Singapore*

[*]Corresponding Author: guokun@nchu.edu.cn

Abstract: Potassium sodium niobate (KNN)-based ceramics exhibit electrical (such as ferroelectric) and photoluminescence (PL) properties and have great application potential in the field of multifunctional optoelectronics. To promote its development in the field of optoelectronics, researchers have been making efforts to improve its photoelectric performance, but mainly through experimental approach with little fundamental theoretical calculations. In this paper, the structural, electronic, and optical properties of $(K_{0.5}Na_{0.5})NbO_3$, $K_{0.375}Na_{0.5}Er_{0.125}NbO_3$ and $K_{0.5}Na_{0.375}Er_{0.125}NbO_3$ material were simulated based on first-principles calculations. The calculation of formation energy reveals that Er is more inclined to replace Na than A-site K. The introduction of Er leads to a decrease in the lattice constant of the structure, and the oxygen octahedron relaxes inward, which is beneficial to the enhancement of ferroelectricity. The orbital hybridization of Er-4f and O-2p leads to a narrower band gap and an increase in absorbance and conductivity. The A-site substitution of Er produces a non-uniform chemical bond environment locally, which is beneficial to the improvement of PL performance. These results provide theoretical insights for doping mechanism of the KNN-Er system and show its potential in the field of optoelectronic applications.

Keywords: KNN · First-principles calculation · Potassium sodium niobate · Electrical and optical properties

1. Introduction

In recent years, propelled by advancements in technology and industry, the field of optoelectronic materials has experienced rapid growth. From optoelectronic sensors and optical communication to optical storage, the applications of optoelectronic devices have deeply permeated various aspects of our lives, profoundly altering our way of life [1-4]. Perovskite-based compounds have garnered significant attention due to their high optical absorption coefficient and large carrier mobility, making them the frontrunners of the new generation of optoelectronic materials [5-11]. Among them, lead zirconate titanate (PZT) based ceramics are commonly used in the manufacturing of optoelectronic devices [12-15]. However, the production, usage, and disposal of these materials may lead to the generation of harmful lead-containing substances, posing potential risks to human health and the environment. With growing emphasis on green environmental standards, lead-based materials are gradually losing competitiveness in future applications. In contrast, environmentally friendly lead-free ceramics exhibit considerable advantages and are promising candidates for achieving integrated optoelectronic functionalities. Potassium sodium niobate (KNN) is considered one of the most promising lead-free piezoelectric ceramic systems due to its good electromechanical coupling properties and low phonon frequency [16-19]. Its susceptibility to the quenching effect of photoluminescence induced by the doping of a large number of heavy metal elements is relatively small, indicating that KNN can serve as a suitable matrix material for rare earth activators, facilitating the realization of multifunctionality with integrated excellent electrical and optical properties. Pure KNN exhibits moderate ferroelectric and dielectric properties, primarily absorbing light in the ultraviolet region, which has limited its applications in the visible and infrared spectral ranges.

Rare earth (RE) elements can confer unique electronic energy levels to ferroelectric materials. Introducing RE ions into the lattice matrix induces ion displacement, thereby altering the material's ferroelectric polarization intensity. Additionally, near the Fermi level, new impurity bands will emerge to regulate bandgaps and photoluminescence (PL) characteristics. In recent years, efforts have been devoted to the development of RE ion-doped KNN systems for optoelectronic multifunctional research and applications. Among them, Erbium (Er) is considered an ideal dopant due to its distinctive electronic structure and level distribution. For example, in the $(K_{0.5}Na_{0.5})_{0.995}Er_{0.005}NbO_3$ ceramic sample [20], the introduction of Er^{3+} exhibits good saturated polarization characteristics and strong photoinduced

coloration response under a 30 V electric field. In the KNN-$x$$Er_2O_3$ ceramic system [21], the inclusion of Er_2O_3 induces a donor doping effect in KNN ceramics. With an Er_2O_3 doping amount of 0.5 mol%, the ceramic exhibits a d_{33} value of 132 pC/N and a k_p value of 0.44. Notably, the ceramic's absorption spectrum and photoinduced luminescence intensity are significantly enhanced by the polarization reorientation during the poling process. Similar observations are found in the Er^{3+} doped $(K_{0.52}Na_{0.48})_{1-x}Li_xNbO_3$ ceramics [22], wherein remarkable enhancements in photoinduced luminescence intensity and ferroelectric properties are observed near the polymorphic phase transition (PPT). In LKNNS-xErNZ-(0.065-x)BZ piezoelectric ceramics [23], the samples exhibit a consistent and stable perovskite structure for x = 0.01 to 0.03. The piezoelectric performance of the samples is enhanced considerably, with d_{33} values surpassing 300 pC/N with a peak value of 500 pm/V. Moreover, intense green photoinduced luminescence is detected during the upconversion and downconversion processes when stimulated by 980 nm and 375 nm laser excitation, respectively. However, current research efforts are primarily focused on the experimental level, with a relative lack of theoretical studies. Further elucidation is needed on the mechanisms underlying the influence of Er element doping on the structure, electrical, and optical responses of KNN.

This study employs first-principles calculations based on density functional theory to simulate the changes in crystal structure, electrical, and optical properties of KNN system before and after doping with Er element. The impact of crystal structure distortions induced by Er substitution at the A-site (replacing K and Na sites) on ferroelectric polarization is systematically analyzed. By integrating information from band structures and density of states (DOS) plots, variations in atomic energy levels and orbital hybridization are investigated. Additionally, electron redistribution and atomic bonding states before and after Er doping are further analyzed using charge density maps, Mulliken charges, and overlap population, to assess atomic charge transfer. Finally, changes in dielectric function and absorbance are discussed to elucidate the influence of Er doping on the dielectric and optical responses of KNN ceramics. This study provides a detailed analysis of the atomic and electronic structural changes of Er within the KNN lattice, offering theoretical support for future explorations into Er doping in the KNN matrix.

2. Computational Details

A first-principles calculation based on density functional theory (DFT) was performed on the superelement model using the CASTEP module integrated within the Materials Studio software [24, 25]. To address the impact of exchange-correlation energy and strong Coulomb repulsion between multiple electrons in the system, the PBE function of generalized gradient approximation (GGA + U) was employed [26]. The Hubbard U values of Nb and Er atoms were also calculated, resulting in 4 eV and 6 eV, respectively [27, 28]. The lattice parameters for the orthorhombic structure of $KNbO_3$ were obtained from the crystal data open library Findit, as shown in Table 1. By employing the supercell method, the $KNbO_3$ monomer was expanded along the X, Y, and Z axes by a factor of 2×2×2, creating a $KNbO_3$ crystal structure comprising 40 atoms.

Table 1 Lattice parameters of orthorhombic $KNbO_3$.

Parameter	Value			
Lattice parameters	a = 3.97408	b = 5.69645	c = 5.72255	
	α = β = γ = 90°			
Space group	Amm2			
Atomic coordinate position	K	0	0	0
	Nb	0.5	0	0.5155
	O	0	0	0.4810
	O	0.5	0.2527	0.2298

The substitution of four K atoms with four Na atoms in a random manner was carried out, and the most stable structure was selected as the crystal model for KNN, as illustrated in Fig. 1(a). A random substitution of a single K atom or Na atom was performed to establish the doping model inclusion of an Er atom, as illustrated in Fig. 1(b-c). During the self-consistent calculation, a plane wave cutoff energy of 610 eV was utilized, and a 4×4×4 k-point grid was selected for the Brillouin zone integral (BZ). Throughout the structural optimization process, the energy convergence difference was less than 1.0×10^{-5} eV/atom, the interaction force difference between atoms was less than 0.03 eV/Å, the internal stress difference was less than 0.05 GPa, and the moving distance difference was less than 0.001 Å.

3. Results and discussion

3.1. *Crystal structure*

The lattice parameters and volume variations of pure KNN and Er-doped KNN structures were computed and presented in Table 2. The calculated lattice parameters obtained are slightly higher than the experimental values at room temperature, with an error of approximately 0.73% [29]. This shows a good agreement between the overall computational results and experimental data, indicating the reliability of the calculations. However, there are still some approximations and errors in the results. This is because the GGA + PBE function used in the calculation has a biased effect on the self-interaction of electrons, which will lead to the delocalization of electrons and make the lattice parameters larger than the actual values. The significant reduction in lattice parameters when Er replaces the A site in KNN can be understood through the inherent properties of the doped element and the structural phase transition of the system. Due to the differences in radius and valence state between Er and K/Na atoms, the doped Er deviates from the ideal positions, resulting in larger lattice distortions. Although the equilibrium lattice parameters of the distorted structure are very similar to those of the undistorted structure, a slight contraction in the volume of the KNN structure caused by the distortion is still observed.

In addition, the degree of structural distortion can also be quantitatively assessed from bond length distributions, which are closely related to most physical and chemical properties. The crystal structure information is introduced using structural analysis visualization software (VESTA), as shown in Fig. 1(d, e, f), where each unit contains a NbO_6 octahedron. The plane perpendicular to the a-axis is the vertical plane, and the four oxygen atoms in this plane are referred to as planar oxygen (O_{II}). Additionally, the two remaining oxygen atoms located on other planes, above and below, are labeled as vertex oxygen (O_I). With the doping of Er, the B-site Nb moves along the [100] direction, leading to a significant decrease in the length of the Nb-$O_{I,1}$ bond and a significant increase in the length of the Nb-$O_{I,2}$ bond, ultimately resulting in lattice volume contraction. This phenomenon may potentially cause a reduction in the dipole moment between the central Nb and O atoms.

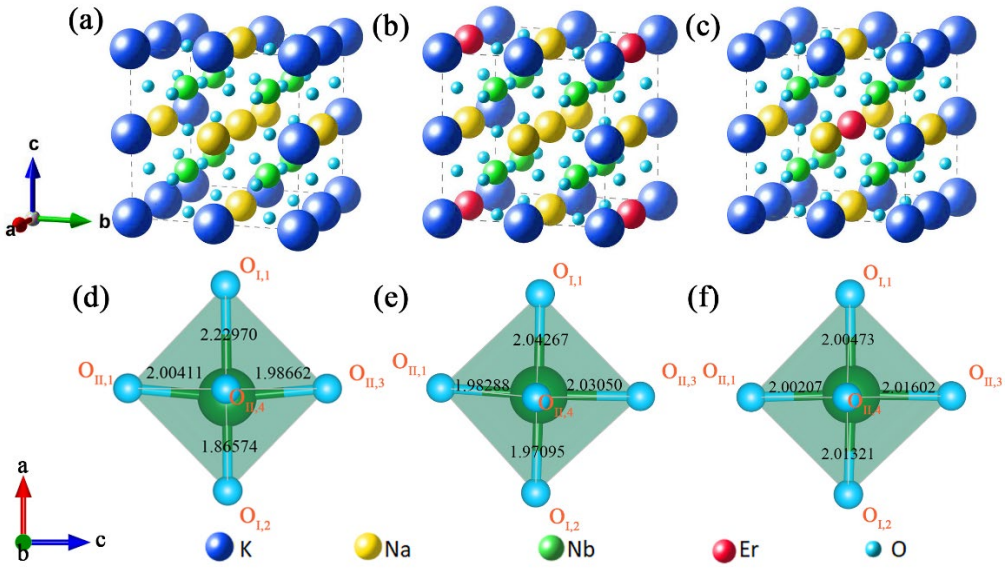

Fig. 1 (a) The pure KNN structure, (b, c) The Er-substituted KNN structures in which an Er atom was randomly substituted for a single K or Na atom, respectively, (d, e, f) The variations in the unit oxygen octahedral structures and bond lengths corresponding to each case are presented.

3.2. *Formation energy of doped elements*

The formation energy of doped elements represents the energy required for the doped atoms to occupy the lattice position of the original atoms [30]. A lower calculated value indicates that the doped atoms can more easily replace the original atoms. As shown in Table S1, the formation energy required for Er substitution of Nb in the B-site of the crystal lattice is significantly higher than that associated with Er replacing K or Na in the A-site, which suggests that Er preferentially substitutes K or Na atoms located in the A-sites of the crystal lattice. To analyze Er substitution at the A-site of the crystal lattice, we calculated the formation energy for Er replacing K and Na atoms in KNN. The expression for doping

formation energy is as follows:

$$E_f(Er \to K) = E(Er \to K) - E(KNN) + \mu_K - \mu_{Er}, \quad (1)$$

$$E_f(Er \to Na) = E(Er \to Na) - E(KNN) + \mu_{Na} - \mu_{Er}. \quad (2)$$

E ($Er \to K$) and E ($Er \to Na$) represent the energy of the most stable structure obtained when the Er atom replaces the K atom or the Na atom, respectively. E (KNN) is the energy of pure KNN structure, μ_{Er}, μ_K, and μ_{Na} represent the chemical potential of each Er, K, and Na atom in the system, respectively.

The formation energy is primarily determined by the difference in ionic radii and charge between the doping atom and the host atom. The lower the difference between the two, or the lower energy after the substitution, the easier it is for the doping atom to enter the lattice and replace the host atom. The ionic radius of Er^{3+} is 0.081 nm, which is smaller than that of K^+ (0.133 nm) and Na^+ (0.095 nm) in the KNN lattice. The difference in ionic radius between Er^{3+} and Na^+ is smaller than between Er^{3+} and K^+. Er has a +3 valence, while K and Na have a +1 valence, resulting in the same charge difference. Hence, Er is more likely to replace A-site Na. We carried out quantitative analysis by calculating the formation energy, which demonstrated that replacing Na with Er resulted in a lower formation energy and a more stable structure. This conclusion supports the qualitative analysis, and the results are presented in Table 3.

Table 2 Lattice constants and volume values of KNN and Er-doped KNN structures after optimization.

Compound	Method	a (Å)	b (Å)	c (Å)	V (Å^3)
	Exp.	7.95600	7.95600	7.86200	497.648
$K_{0.5}Na_{0.5}NbO_3$	Present	8.13774	8.13774	7.91941	524.418
$K_{0.375}Na_{0.5}Er_{0.125}NbO_3$ (Er replaces K-site)	-	8.01913	8.03005	8.02282	516.621
$K_{0.5}Na_{0.375}Er_{0.125}NbO_3$ (Er replaces Na-site)	-	8.03444	8.03444	8.03081	518.405

Table 3 Generation energy information of KNN doped by Er (eV)

	E ($Er \to K$) ($\times 10^4$)	E ($Er \to Na$) ($\times 10^4$)	E (KNN) ($\times 10^4$)	μ_K ($\times 10^2$)	μ_{Na} ($\times 10^3$)	μ_{Er} ($\times 10^3$)	E_f
Er→K	-3.652228	-	-3.222008	-7.914454	-	-5.091891	-1.75
Er→Na	-	-3.600507	-3.222008	-	-1.308785	-5.091891	-1.88

3.3. *Band structure*

The band structures obtained from G-Z-T-Y-G-S-R-Z high symmetric K-point path simulation are presented in Fig. 2(a-c). All three band structures are characterized by dense and flat bands, with the valence band maximum (VBM) and conduction band minimum (CBM) located at the G point, indicating direct band gaps. The electrons only need to absorb energy to transition to the conduction band to produce conductive electrons and holes, which are easier to transition than the indirect band gap. The results demonstrate that compared to the undoped structure shown in Fig. 2(a), the conduction band and valence band of the Er-doped KNN structures in Fig. 2(b-c) shift towards lower energies. Specifically, the energy ranges for the conduction band and valence band of the pure KNN structure are 2 eV to 25 eV and -6 eV to 0 eV, respectively. In contrast, the two Er-doped KNN structures exhibit energy ranges in the conduction and valence bands from -0.5 eV to 20 eV and -8 eV to -2 eV, respectively. The Fermi level intersects with the bottom of the conduction band, forming an impurity band nearby. The Er atom replaces the K and Na sites, and after satisfying the basic coordination electrons, there are more free electrons. This leads to the introduction of additional electrons in the system. The electron concentration is greater than the hole concentration, and the Fermi level shifts to the conduction band. The band gap corresponds to the transition from the top of the valence band, occupied by the O-2p electronic state, to the bottom of the conduction band, dominated by the Nb-4d state. Adding Er results in a narrower band gap and less energy required for electron transition, ultimately leading to enhanced conductivity compared to pure KNN. The band gap of pure KNN is 2.262 eV, and the band gap of doped KNN is 1.868 eV (Er instead of K) and 1.778 eV (Er instead of Na). For pure KNN, the computed bandgap value is lower than the experimental value of 3.11 eV, which is a common issue of underestimated bandgap in first-principles calculations [31]. The main reason is that the entire computation is based on the foundation of density functional theory, which neglects the discontinuity of exchange-correlation

potential among electrons and underestimates the correlation among excited electrons in a multi-particle system. However, this does not affect our analysis.

3.4. *Density of state*

From the total density of states (DOS) shown in Fig. 2(d, e, f), it can be observed that upon Er doping, the Fermi level of KNN shifts towards higher energy conduction bands, resulting in a reduction of the bandgap, which is consistent with the band calculation results. The partial density of states (PDOS) shown in Fig. 2(g-i) suggests that p-d hybridization occurs between O-2p and Nb-4d orbitals, while s-p hybridization takes place between s and p orbitals of a small number of K and Na atoms and O atom. These findings suggest the presence of strong covalent bonds between O and Nb atoms in pure KNN. Compared to Na atoms, the hybridization between K and O atoms is stronger, facilitating the formation of weak covalent and ionic bonds. As illustrated in Fig. 2(h), the substitution of Er for K leads to an increase in the hybridization between Na atoms and O atoms, while the hybridization between K atoms and O atoms decreases. In contrast, as demonstrated in Fig. 2(i), when Er replaces Na, a similar trend in hybridization between these atoms is found. In both scenarios, new overlapping orbitals of Er-4f and O-2p are generated, which may result in the formation of ionic bonds between Er and O atoms.

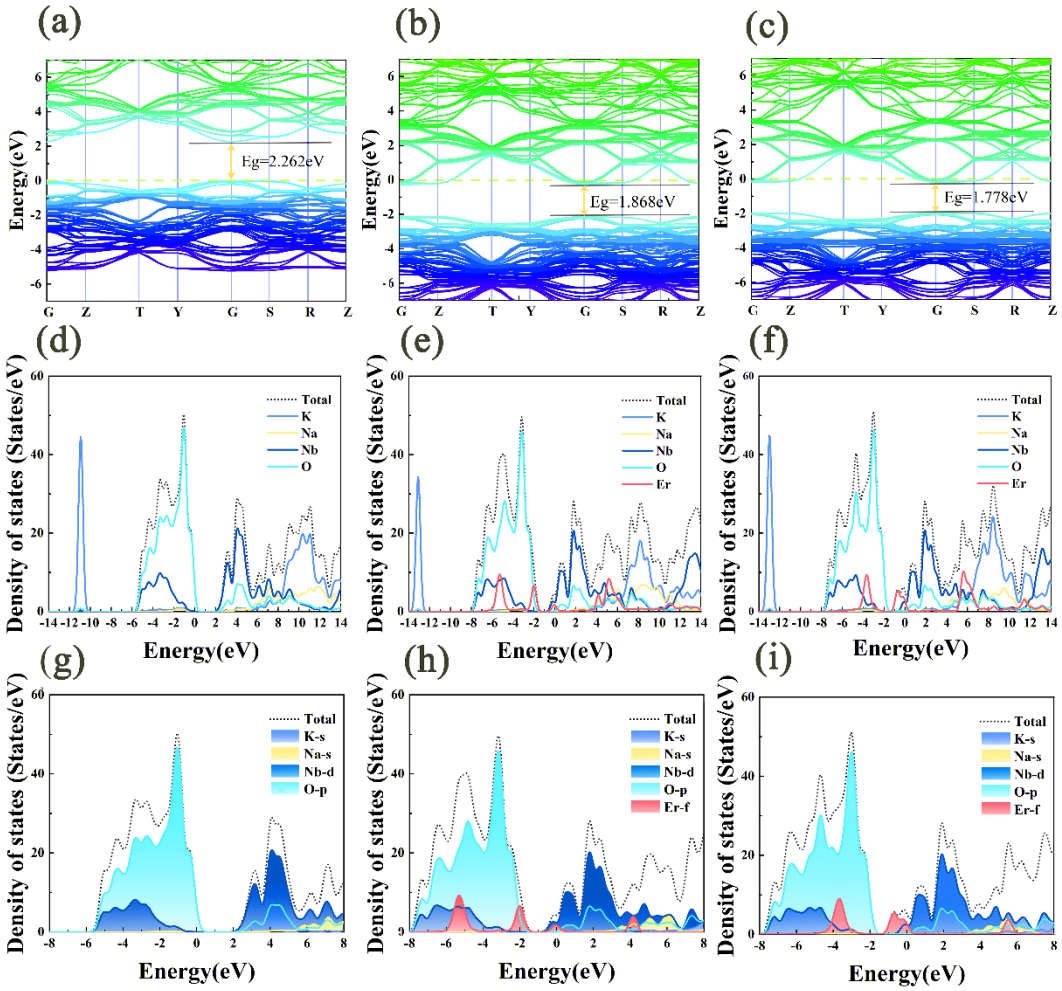

Fig. 2 The band structure and density of states for three distinct structures: (a, d, g) Pure KNN, (b, e, h) KNN with Er substitution at K sites, (c, f, i) KNN with Er substitution at Na sites.

3.5. *Electron charge density*

To investigate changes in chemical bond types and strengths between atoms in the KNN structure before and after doping, the 3D charge density distribution was calculated along the (100) crystal plane of pure KNN and Er-doped KNN. As revealed in Fig. 3(a, c), the interaction between K or Na ions and O ions

exhibits the characteristics of weak covalent bonds and ionic bonds. When Er substitutes for K or Na, ionic and weak covalent bonds form between Er and O ions, as shown in Fig. 3(b, d). Quantitative analysis results presented in Table S2 show that K, Na, and Nb atoms all lose electrons, while O presents an electron gain phenomenon for pure KNN. Under Er doping, Er also exhibits electron loss. This indicates that some electrons in the structure are transferred to O atoms, forming ionic bonds. Table S2 presents the overlapping charge populations for the three structures, where positive values represent the presence of covalent bonds, negative values indicate the presence of antibonds between atoms, and 0 represents ideal ionic bonding [32]. Table S2 reveals that the bond populations of Nb-O in KNN fall within the positive range of 0.68 to 0.92, indicating a strong covalent bond. On the other hand, both structures of KNN doped with Er exhibit an overall Er-O bond population close to zero, suggesting that the Er-O bond primarily consists of ionic and weak covalent bonds.

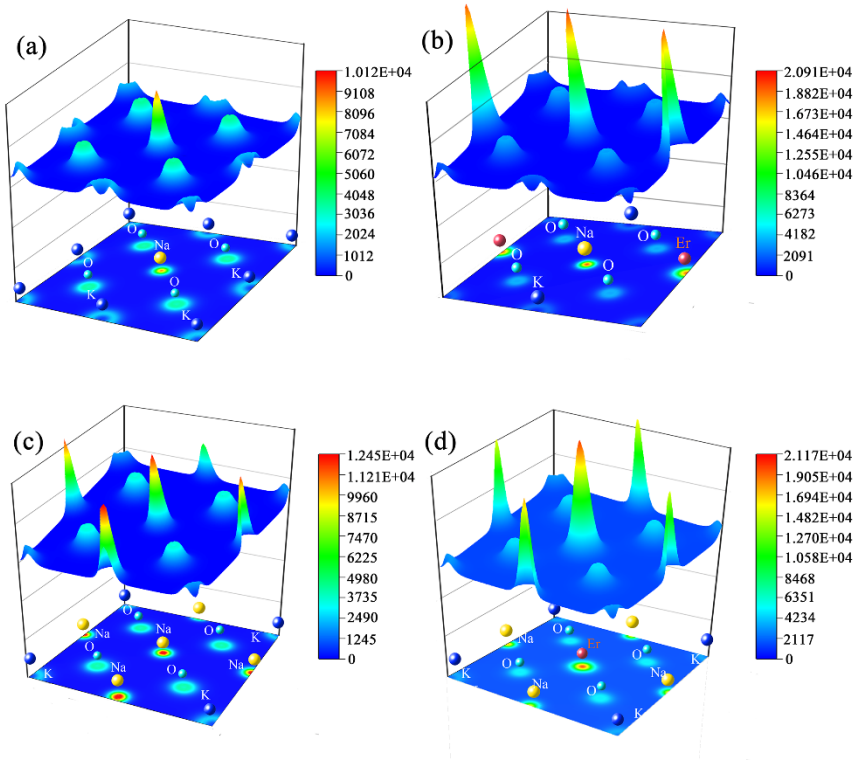

Fig. 3 The 3D charge density distribution on (100) plane: (a, c) Pure KNN, (b) Er substituted K atom, (d) Er substituted Na atom.

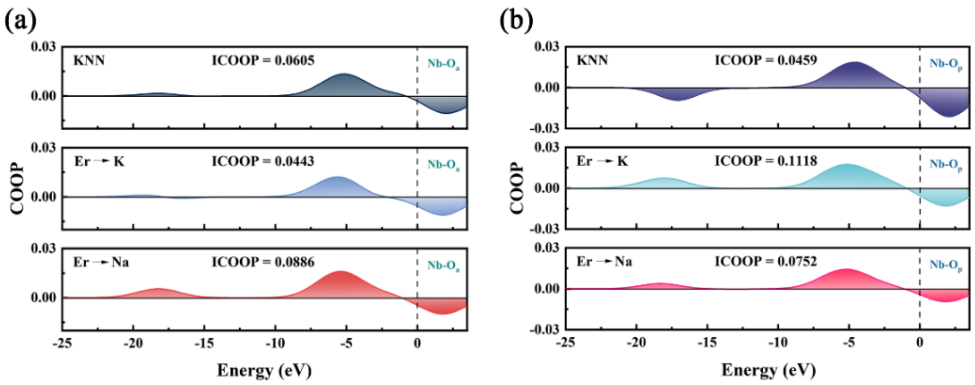

Fig. 4 COOP of Nb-O interaction in pure KNN structure and K/Na site doped KNN-Er structure. (a) Nb-O_a, (b) Nb-O_p, O_a and O_p represent the vertex oxygen atom and the plane oxygen atom in the oxygen octahedral structure, respectively.

After A-site substitution, the relatively small ionic radius of Er leads to a tighter local electron configuration between Er and the surrounding four O anions. The results in a locally non-uniform

chemical bond environment on the A-site plane, as shown in Fig. S1(b, e). However, by comparing the charge density maps of the B-site plane in Fig. S1(c, f, g), the uniformity of the chemical bonds around the Nb remains unchanged on the B-site plane. The significant difference in bond strength on different planes indicates that the A-site substitution of Er has a localized impact and exhibits good energy stability on the A-site. Moreover, the presence of local non-uniform chemical bond environments is beneficial for the PL performance of the system.

The integrated COOP value (ICOOP) provides a way to quantify the bonding strength. As shown in Fig. 4, when Er replaces the Na site, the bond energies of Nb-O_a and Nb-O_p are enhanced, which may lead to the distortion of the O_p plane and the Nb-O_6 octahedron near it. This is consistent with the B-site ion shift along the [100] direction shown in Fig. 1(f), the bond lengths of $O_{I,\,1}$ and $O_{II,\,1}$ decrease, and the symmetry of the crystal structure is improved.

3.6. *Optical properties*

The lattice constants of KNN exhibit different values in a, and c directions before and after doping, reflecting the anisotropic optical properties [33, 34]. The influence of Er doping on the optical properties of KNN was analyzed by calculating the dielectric constants and absorption coefficients of pure KNN and Er-doped KNN along the x and z axes. The static dielectric constant ε_r can be obtained when the photon energy equals zero [35-37].

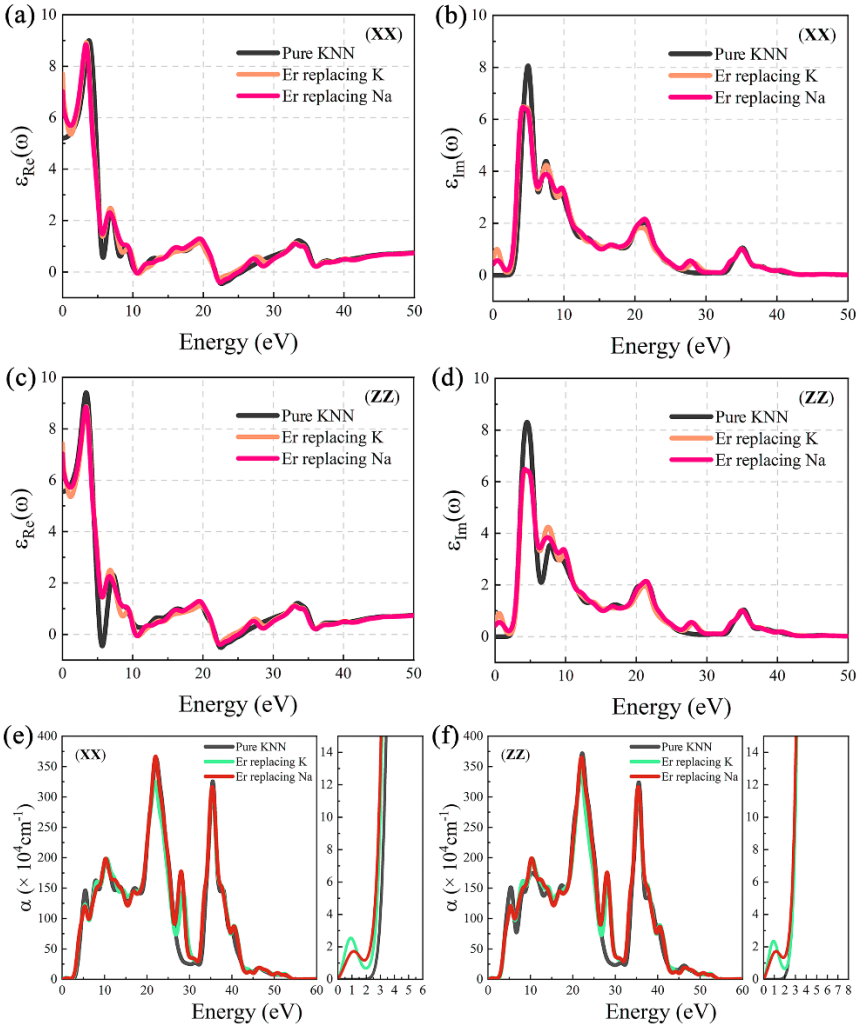

Fig. 5 (a, b) Real and imaginary parts of the dielectric function along the X-axis for pure KNN and Er-doped KNN. (c, d) Real and imaginary parts of the dielectric function along the Z-axis for pure KNN and Er-doped KNN. (e, f) Variation of the absorption coefficient along the X and Z axes for pure KNN and Er-doped KNN.

Fig. 5(a, c) presents the genuine part of the dielectric function, where the εr values for pure KNN

along the x and z axes are 5.2 and 5.56, respectively. After Er doping, the εr values of the KNN structure significantly increase, indicating enhanced electronic polarization. Specifically, for Er substitution at the K site, the εr values along the x and z axes are 7.7 and 7.43, respectively. For Er substitution at the Na site, the εr values are both 7.03. In addition, the pure KNN exhibits a main peak at 3.71 eV, while the two main peaks of Er substitution at the K site are at 0.01 eV and 3.35 eV, and the two dominant peaks of Er substitution at the Na site are at 0.01 eV and 3.28 eV. The various peaks in the imaginary part of the dielectric function are associated with band structures and transitions between energy levels [38-41]. As shown in Fig. 5(b, d), the imaginary part of the dielectric function for pure KNN along the x and z axes corresponds to optical transitions from O-2p to Nb-4d states. After doping, Er-doped KNN shows slight peaks at lower photon energies, with the two main peaks corresponding to energy level transitions from Er-4f to O-2p states and from O-2p to Nb-4d states. Fig. 5(e, f) shows the variation of the absorption coefficient. The introduction of Er leads to changes in the absorption of incident light in KNN, and nearly identical absorption spectra are obtained in different directions. The local tangent lines of the absorption curve of pure KNN yield an intercept at 2.2 eV on the x-axis, indicating that the absorption edge of pure KNN is around 2.2 eV, within the visible light absorption range of 1.6-3.2 eV, consistent with the previously calculated bandgap values. After doping, the absorption edge shifts towards lower energies, and new absorption peaks emerge, indicating that the optical response of KNN in the visible light range is significantly enhanced through Er doping.

4. Conclusions

The structure, electrical and optical properties of $(K_{0.5}Na_{0.5})NbO_3$, $K_{0.375}Na_{0.5}Er_{0.125}NbO_3$ and $K_{0.5}Na_{0.375}Er_{0.125}NbO_3$ crystals were studied using first-principles calculations. Upon Er doping, the crystal structure of KNN undergoes distortion, resulting in volume contraction. Er is more likely to replace the A-site Na, causing a decrease in both the energy and the bandgap of the structure and a shift of the Fermi level towards the conduction band direction. The charge density analysis shows that KNN possesses strong Nb-O covalent bonds both before and after doping, whereas Er forms new ionic and weak covalent bonds with O after doping. Furthermore, Er doping was found to improve the absorbance and PL performance of KNN. The density of states and dielectric function analysis indicated that the improved optical properties were related to the hybridization of Er-4f and O-2p.

Supplementary Information

The online version contains supplementary material available.

Acknowledgments

This project was partially supported by the National Natural Science Foundation of China (Grant No. 52002164, No. 52060020, No. 52162018, No. 52162019), and the Natural Science Foundation of Jiangxi Province of China (Grant No. 20202BABL204013). The author from IMRE acknowledges partial supports from A*STAR, under RIE2020 AME Programmatic Fund (Grant No. A20G9b0135), Singapore.

Author contributions

Material preparation and data curation were performed by Z.G. and H.Y. Supervision, writing-reviewing were performed by K.G., editing and investigation were performed by K.F., B.X., Z.L., P.M., J.L., K.Y. and F.T. The first draft of the manuscript was written by Z.G., and all authors commented on previous versions of the manuscript. All authors read and approved the final manuscript.

Data availability

No datasets were generated or analysed during the current study.

Declarations

Competing Interests: The authors declare no competing interests.

References

1. B. Xie, Z. Chen, L. Ying, F. Huang, Y. Cao, InfoMat **2**(1), 57-91 (2020)

2. Y. Xing, Y. Xu, Q. Wu, G. Wang, M. Zhu, J. Mater. Chem. C **9**(2), 439-455 (2021)
3. N. Huo, G. Konstantatos, Adv. Mater. **30**(51), 1801164 (2018)
4. L.-R. Zou, D.-D. Sang, Y. Yao, X.-T. Wang, Y.-Y. Zheng, N.-Z. Wang, C. Wang, Q.-L. Wang, Rare Met. **42**(1), 17-38 (2023)
5. S. Dong, Z. Y. Hu, P. Wei, J. Han, Z. Wang, J. Liu, B. L. Su, D. Zhao,Y. Liu, Adv. Mater. **34**(37), 2204342 (2022)
6. Y. Ji, W. Xu, I. L. Rasskazov, H. Liu, J. Hu, M. Liu, D. Zhou, X. Bai, H. Ågren, H. Song, Appl. Phys. Rev. **9**(4), 041319 (2022)
7. L. Li, S. Ye, J. Qu, F. Zhou, J. Song, G. Shen, Small **17**(18), 2005606 (2021)
8. F. Liu, S. Sidhik, M. A. Hoffbauer, S. Lewis, A. J. Neukirch, V. Pavlenko, H. Tsai, W. Nie, J. Even, S. Tretiak, Nat. Commun. **12**(1), 673 (2021)
9. X. Liu, S. Ren, Z. Li, J. Guo, S. Yi, Z. Yang, W. Hao, R. Li, J. Zhao, Adv. Funct. Mater. **32**(38), 2202951 (2022)
10. Z. Liu, X. Liu, B. Sun, X. Tan, H. Ye, J. Zhou, Z. Tang, T. Shi, G. Liao, Adv. Mater. Technol. **5**(8), 2000260 (2020)
11. Z. Xue, Y. Xu, C. Jin, Y. Liang, Z. Cai, J. Sun, Nanoscale **15**(10), 4653-4668 (2023)
12. G. Chen, Y. Zhang, Q. Zhang, Y. Lu, Y. He, Ceram. Int. **46**(10), 15061-15065 (2020)
13. G. Chen, K. Zou, Y. Yu, Y. Zhang, Q. Zhang, Y. Lu, Y. He, Ceram. Int. **46**(4), 4148-4153 (2020)
14. Z. Han, Y. Chang, B. Zhang, W. Wang, S. Wang, W. Zhai, J. Wang, Ceram. Int. **48**(16), 24114-24118 (2022)
15. F. Zheng, P. Zhang, X. Wang, W. Huang, J. Zhang, M. Shen, W. Dong, L. Fang, Y. Bai, X. Shen, Nanoscale **6**(5), 2915-2921 (2014)
16. H. Du, F. Tang, F. Luo, D. Zhu, S. Qu, Z. Pei, W. Zhou, Mater. Res. Bull. **42**(9), 1594-1601 (2007)
17. M. Feizpour, H. B. Bafrooei, R. Hayati, T. Ebadzadeh, Ceram. Int. **40**(1), 871-877 (2014)
18. L. Qiao, G. Li, H. Tao, J. Wu, Z. Xu, F. Li, Ceram. Int. **46**(5), 5641-5644 (2020)
19. W. Yang, P. Li, S. Wu, F. Li, B. Shen, J. Zhai, Ceram. Int. **46**(2), 1390-1395 (2020)
20. Y. Zhang, L. Luo, K. Li, W. Li, Ceram. Int. **44**(1), 1086-1090 (2018)
21. Y. Zhao, X. Yuan, Y. Zhao, H. Zhou, J. Li, H. Jin, Mater. Lett. **162**, 226-229 (2016)
22. Y. Zhao, Y. Ge, X. Yuan, Y. Zhao, H. Zhou, J. Li, H. Jin, J. Alloys Compd. **680**, 467-472 (2016)
23. Q. Liu, E. Pan, H. Deng, F. Liu, Ceram. Int. **49**(10), 14981-14988 (2023)
24. M. Segall, P. J. Lindan, M. a. Probert, C. J. Pickard, P. J. Hasnip, S. Clark, M. Payne, J. Phys.: Condens. Matter **14**(11), 2717 (2002)
25. V. Milman, B. Winkler, J. White, C. Pickard, M. Payne, E. Akhmatskaya, R. Nobes, Int. J. Quantum Chem. **77**(5), 895-910 (2000)
26. J. P. Perdew, Y. Wang, Phys. Rev. B **38**(17), 12228 (1988)
27. T. Usman, G. Murtaza, H. Luo, A. Mahmood, J. Supercond. Novel Magn. **30**, 1389-1396 (2017)
28. V. I. Anisimov, I. Solovyev, M. Korotin, M. Czyżyk, G. Sawatzky, Phys. Rev. B **48**(23), 16929 (1993)
29. D. Yang, L. Wei, X. Chao, Z. Yang, X. Zhou, Phys. Chem. Chem. Phys. **18**(11), 7702-7706 (2016)
30. J.-i. Tani, H. Kido, Intermetallics **16**(3), 418-423 (2008)
31. S.-L. Zhou, X. Zhao, X.-P. Jiang, X.-D. Han, Chin. J. Struct. Chem. **31**(8), 1095-104 (2012)
32. R. S. Mulliken, J. Chem. Phys. **23**(10), 1833-1840 (1955)
33. C. I. Zandalazini, J. N. Sanchez, E. A. Albanesi, Y. Gupta, P. Arun, J. Alloys Compd. **746**, 9-18 (2018)
34. Y. Li, C. Liu, H. Yu, F. Wang, X. Zhang, Vacuum **159**, 218-227 (2019)
35. B. Liu, M. Gu, X. Liu, Appl. Phys. Lett. **91**(17), 172102 (2007)
36. M. R. Osanloo, M. L. Van de Put, A. Saadat, W. G. Vandenberghe, Nat. Commun. **12**(1), 5051 (2021)
37. P. Broqvist, A. Pasquarello, Appl. Phys. Lett. **90**(8), 082907 (2007)
38. K. Liu, H. Fan, P. Ren, C. Yang, J. Alloys Compd. **509**(5), 1901-1905 (2011)
39. M.-Q. Cai, Z. Yin, M.-S. Zhang, Appl. Phys. Lett. **83**(14), 2805-2807 (2003)
40. M. Zhong, Q.-J. Liu, C.-L. Jiang, F.-S. Liu, B. Tang, X.-J. Peng, J. Phys. Chem. Solids **121**, 139-144 (2018)
41. M. Saeed, A. Ali, I. U. Haq, S. Muhammad, A. R. Chaudhry, A. ur Rehman, Z. Ali, S. M. Siddeeg, I. Khan, Mater. Sci. Semicond. Process. **139**, 106364 (2022)